Check for updates

Advanced Optical Materials

ADVANCED OPTICAL MATERIALS
www.advopticalmat.de

RESEARCH ARTICLE OPEN ACCESS

Spectral Reconstruction Using Broadband Inkjet-Printed Optical Filters

Leonardo Baini[1] | Qihao Jin[2] | Qiaoshuang Zhang[2] | Guillaume Gomard[3] | Uli Lemmer[2] | Paolo Bartolini[1] | Andrea Taschin[1,4] | Diederik S. Wiersma[1,5,6] | Renato Torre[1,5] | Alice Boschetti[1,6]

[1]European Laboratory for Non-Linear Spectroscopy, University of Florence, Sesto Fiorentino, Italy | [2]Light Technology Institute, Karlsruhe Institute of Technology (KIT), Karlsruhe, Germany | [3]Carl Zeiss AG, Zeiss Innovation Hub, Eggenstein-Leopoldshafen, Germany | [4]Consiglio Nazionale delle Ricerche, Istituto Nazionale di Ottica, CNR-INO, Sesto Fiorentino, Italy | [5]Dipartimento Di Fisica ed Astronomia, Università di Firenze, Sesto Fiorentino, Italy | [6]Istituto Nazionale di Ricerca Metrologica (INRiM), Torino, Italy

Correspondence: Leonardo Baini (leonardo.baini@lens.unifi.it) | Qihao Jin (qihao.jin@kit.edu)

Received: 25 August 2026 | **Revised:** 20 September 2026 | **Accepted:** 30 September 2026

Keywords: convex optimization | Inkjet-printed filters | optical filters | optics | reconstructive spectroscopy | spectroscopy

ABSTRACT

Reconstructive spectroscopy offers a promising route toward miniaturization by replacing dispersive optics with computational recovery from encoded measurements, but existing implementations typically rely on complex nanofabrication and highly decorrelated encoding elements, limiting manufacturability and robustness. Here, we demonstrate a reconstructive spectrometer based on inkjet-printed interferometric optical filters featuring a minimalist tri-layer architecture and high optical throughput. Contrary to prevailing design principles, we show that smooth, strongly correlated filter responses can nonetheless enable accurate spectral reconstruction over a 400 nm visible bandwidth. By adaptively selecting optimized subsets of filters using a custom genetic algorithm, the system exploits the high signal-to-noise ratio of correlated encoders while maintaining reconstruction fidelity. In addition, we introduce a calibration and reconstruction framework that requires only minimal a priori knowledge of the measured spectra, increasing the viability of practical deployment of reconstructive spectrometers. The resulting procedure combines scalable fabrication, adaptive encoding, and robust reconstruction, with a strong basis of versatile and manufacturing-ready encoding elements.

1 | Introduction

Compact, high-resolution spectrometers are key enabling components for a wide range of emerging technologies, including distributed environmental sensing, industrial process monitoring, point-of-care diagnostics, and wearable health devices. In these contexts, spectrometers must not only achieve high spectral resolution and broad bandwidth, but also be scalable, robust, and compatible with low-cost, portable platforms. These requirements have motivated intense research efforts aimed at miniaturizing spectrometers beyond the limits imposed by conventional dispersive optics. Among the most promising approaches is reconstructive spectroscopy, in which spectral information is encoded by a set of optical elements and subsequently recovered using computational algorithms. By replacing standard diffractive elements with arrays of spectral encoders, reconstructive spectrometers offer a pathway toward ultracompact form factors while maintaining high performance [1]. Types of optical encoders include resonating cavities [2, 3], quantum dots [4, 5], thin films [6], metasurfaces [7–9], nanowires [10], liquid crystals [11], integrated photonics platforms [12], and disordered systems [13]. Some of the most recent and notable examples include reconstructive spectrometers based on multi-resonant cavities [14] and a metasurface-metalens combination [15] with achieved

This is an open access article under the terms of the Creative Commons Attribution License, which permits use, distribution and reproduction in any medium, provided the original work is properly cited.
© 2026 The Author(s). *Advanced Optical Materials* published by Wiley-VCH GmbH

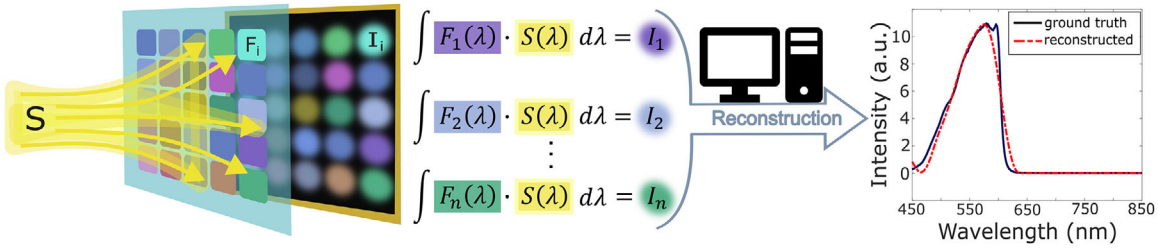

FIGURE 1 | Representation of the process of spectral reconstruction, from left to right: first, the unknown signal **S** interacts with an array of encoding elements, which generates n signals I_i for each transmittance $\mathbf{F}_i$ of the encoders. Effectively, the information contained in **S** is transduced into a vector of measurements **I** by integration over the sensor bandwidth. These values, together with the calibration of the encoder matrix, are then used as input for the post-processing algorithms to solve the given underdetermined system of equations and reconstruct the spectrum.

bandwidths of several hundreds of nanometers and resolutions of ~0.5 nm in the visible or infrared range.

Despite impressive demonstrations, most existing reconstructive spectrometers rely on encoding elements that require complex nanofabrication, precise multilayer deposition, or subwavelength patterning. In addition, these encoding elements must exhibit low mutual spectral correlation, which significantly complicates the filter design and increases fabrication complexity. Here, we introduce a notably different approach to reconstructive spectroscopy based on inkjet-printed arrays of simple triple-layer interferometric filters. These filters act as compact spectral encoding elements with smooth, slowly varying, and strongly correlated transmission responses, in direct contrast to conventional design strategies [16, 17]. Surprisingly, we show that such highly correlated encoding elements can nonetheless enable accurate spectral reconstruction over a 400 nm bandwidth in the visible, representing a significant step over previously reported reconstructive spectrometers [18–20] using comparably simple optical components. Our approach combines scalable fabrication, adaptive encoding, and data-efficient reconstruction within a unified framework. Interferometric filters are fabricated by inkjet printing, enabling scalable, low-cost, and mask-free production without the need for sub-micrometer patterning or complex multilayer stacks. Rather than enforcing the high decorrelation needed for generalist encoding matrices, we tailor optimized subsets of encoding elements to the target spectral content using a custom genetic algorithm. This strategy allows the system to exploit the high average transmittance and favorable signal-to-noise properties of correlated filters while maintaining reconstruction fidelity. Finally, we introduce a calibration and reconstruction framework that requires minimal a priori knowledge of the measured spectra, addressing an important barrier to the practical deployment of reconstructive spectroscopy: the determination of the optimal algorithmic parameters prior to operation.

The operating principle of a reconstructive spectrometer is illustrated in Figure 1. An unknown input spectrum $\boldsymbol{S}(\lambda_1, \lambda_2, \ldots, \lambda_n)$ is encoded by an array of M optical filters, each characterized by a distinct transmission function $\mathbf{F}_j\,(\lambda_1, \lambda_2, \ldots, \lambda_n)$, with $j = 1,\ldots, M$. The resulting set of transmitted intensity from the filters forms an M-dimensional vector $\boldsymbol{I}$, which can be related to the input spectrum through a linear forward model: [21–24]

$$\boldsymbol{I} = \mathbf{F} \cdot \boldsymbol{S} \tag{1}$$

where **F** is the M x N matrix containing the pre-calibrated spectral transmittances of all the encoding elements [25–27] with sampling wavelengths $\lambda_1, \lambda_2, \ldots, \lambda_n$. Because the number of measurements M is much smaller than the number N of reconstructed spectral channels, the system is underdetermined and must be solved using optimization techniques that exploit sparsity or compressibility in an appropriate basis [28, 29]. Typically, this operation is modeled as a convex optimization problem, such as LASSO (Least Absolute Shrinkage and Selection Operator) [30], basis pursuit [31], or ridge regression [32].

2 | Results

We first established a reconstruction framework that enables accurate spectral recovery while requiring minimal a priori information about the measured signal. Spectral reconstruction is formulated as a regularized inverse problem, in which the measured intensities are fitted while enforcing sparsity of the reconstructed spectrum on an appropriate basis. Specifically, we minimize:

$$\left|\left|\, \mathbf{F} \cdot \boldsymbol{S} - \boldsymbol{I} \,\right|\right|_2^2 + \gamma \left|\left| \mathrm{DCT}\,(\boldsymbol{S}) \right|\right|_1 \tag{2}$$

where the first term enforces consistency with the measured intensities and the second regularization term promotes sparsity of the spectrum in the Discrete Cosine Transform (DCT) basis. This basis was selected because it constrains solutions to smooth, slowly varying spectral profiles, which are representative of many practical light sources while remaining compatible with compressed sensing principles.

A key challenge in reconstructive spectroscopy is the selection of the regularization parameter γ. Conventional approaches determine γ a posteriori using residual-based methods such as L-curve analysis or cross-validation [33], which require either knowledge of the ground truth or multiple iterations over values of γ. In real-world sensing scenarios, however, the target spectral function is unavailable, and time constraints prohibit the use of such iterative algorithms. To overcome these limitations, we introduce a pre-calibration strategy that links the optimal value of γ to experimentally accessible quantities, namely the spectral bandwidth (or full width at half maximum, FWHM) and the signal-to-noise ratio (SNR). Using the experimentally measured transmittance matrix of the printed filters (Figure 2d), we simulated intensity measurements for Gaussian spectra spanning a

21951071, 0, Downloaded from https://advanced.onlinelibrary.wiley.com/doi/10.1002/adom.71918 by CochraneItalia, Wiley Online Library on [23/10/2026]. See the Terms and Conditions (https://onlinelibrary.wiley.com/terms-and-conditions) on Wiley Online Library for rules of use; OA articles are governed by the applicable Creative Commons License

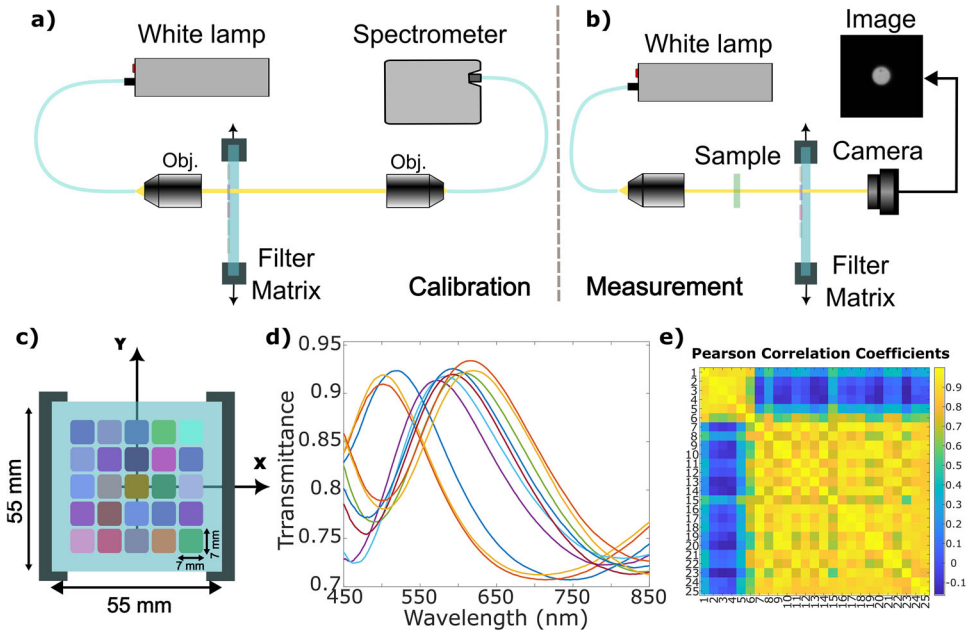

FIGURE 2 | Schematic representation of the experimental setup utilized for calibration (a) and measurement (b) with an example of raw intensity measurement shown. A broadband light source is fiber-coupled to a microscope objective to focus the light onto the filters, which are mounted on an x-y translational stage. During calibration, the transmitted light is collected by another microscope objective, which is fiber-coupled to a spectrometer. During measurement, instead, the transmitted intensity is recorded by a camera after passing through the chosen sample. (c) A schematic representation of the filter matrix. (d) Measured transmittance of the filters. Note that all transmittance values lie above 70%, enabling a very high signal. Here, for clarity, only 10 transmittances out of 25 are shown, the full group is reported in Figure S2. (e) Pearson correlation coefficients of the filter matrix, showing high average correlation between the transmittances of the filters.

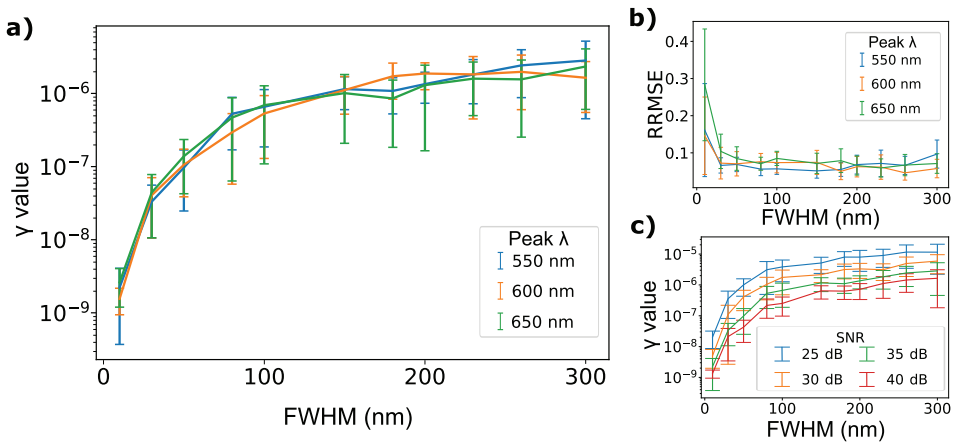

FIGURE 3 | Means of the optimal values for each reconstructed Gaussian spectrum of different spectral bandwidths (or full widths at half maximum, FWHMs), peak wavelengths, and SNRs. (a) Values of γ for an SNR equal to 35 dB. The peak wavelength seems to have very little effect on the optimal value of γ. This result helps narrow the value of γ to a range, but does not indicate an exact value. (b) Means of the RRMSE for each reconstructed Gaussian spectrum of different FWHMs and peak wavelengths for an SNR of 35 dB. (c) Means of the optimal values for each reconstructed Gaussian spectrum of different FWHMs and SNRs for a peak wavelength of 550 nm.

wide range of peak wavelengths, full widths at half maximum, and noise levels. For each case, the optimal γ was determined by minimizing the reconstruction error (using the *dlib* [34] global minima algorithm). This procedure yields a calibration map that provides an informed, first-order estimate of γ using only rough prior knowledge of the spectrum and measurement noise and requires no at-measurement optimization of parameters.

Figure 3a shows the dependence of the optimal regularization parameter γ on the spectral bandwidth for Gaussian spectra at three representative peak wavelengths, assuming an SNR of approximately 35 dB, corresponding to our experimental conditions. Notably, the peak wavelength has only a minor influence on the optimal γ, whereas the spectral bandwidth plays a dominant role. This result significantly speeds up and simplifies parameter

21951071, 0, Downloaded from https://advanced.onlinelibrary.wiley.com/doi/10.1002/adom.71918 by Cochraneltalia, Wiley Online Library on [23/10/2026]. See the Terms and Conditions (https://onlinelibrary.wiley.com/terms-and-conditions) on Wiley Online Library for rules of use; OA articles are governed by the applicable Creative Commons License

TABLE 1 | Optimal γ values for various experimental spectra.

Spectra	Broad White	Broad Red	Broad green	Narrow Red	Narrow Green
Estimated center [nm]	650	660	550	630	550
Estimated FWHM [nm]	260	180	80	10	10
γ value	2e-6	2e-7	3e-8	6e-9	2.5e-9

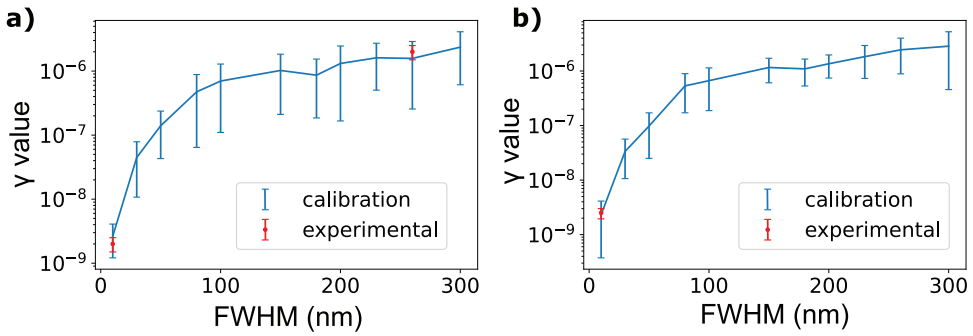

FIGURE 4 | γ-bandwidth relation for Gaussians peaked at (a) 650 nm and (b) 550 nm, initial a priori calibration results shown in blue, optimal parameters found with known ground truth optimization shown in red.

selection, as it allows γ to be estimated primarily from the expected spectral width.

The same calibration procedure provides an estimation of the reconstruction accuracy achievable with the printed filter matrix. As shown in Figure 3b, the average relative root mean square error (RRMSE) across the explored parameter space is mostly below 10%, with consistently better performance for broadband spectra. Narrower spectra are more challenging to reconstruct, reflecting the limited high-frequency content supported by the DCT basis. As expected, the optimal γ increases monotonically with decreasing SNR (Figure 3c), reflecting the increasing importance of regularization in suppressing the effect of noise in fitting. Importantly, this trend enables γ to be adjusted dynamically in response to changes in measurement conditions, enhancing the robustness of the reconstruction. We next applied the calibrated reconstruction framework to experimentally measured intensity data. Spectral measurements were performed using the setup shown in Figure 2b, in which the transmitted light through the filter array was recorded by a camera. A refined optimization of γ was also performed for each experimental spectrum to validate the predictions of the calibration map. The resulting γ values, summarized in Table 1, show excellent agreement with the a-priori estimates for spectra that closely resemble Gaussian profiles (Figure 4). This agreement confirms that the proposed calibration strategy provides reliable parameter estimates even in the absence of exact spectral knowledge.

Although the full array consists of 25 filters, we observed that reconstruction accuracy improves when using only a subset of the available filters. This behavior is counterintuitive from the perspective of traditional sensing, where additional measurements are generally expected to improve reconstruction quality. Here, however, the high degree of correlation between filter transmittances (Figure 2e) means that redundant information can degrade numerical stability.

Given the large number of possible combinations, a genetic algorithm was employed to determine, within a reasonable computing time, the optimal subset of filters to keep (Figure 5). The algorithm was designed to investigate the filter combination space, both by checking random combinations, as well as improving promising ones, and to search for the optimal number of filters to utilize [35]. After 300 generations, the algorithm consistently converges toward compact filter sets comprising seven to fifteen elements, depending on the target spectrum.

The transmittances of the chosen filters can be seen in the right column of Figure 6, alongside the corresponding reconstructed spectra in the left column, together with the relative ground truth signals, measured with a commercial spectrometer. Interestingly, the filters chosen by the genetic algorithm change in both type and number for each spectrum. In several cases, reconstructions using optimized subsets significantly outperform those obtained with the full filter array, showing the advantage of adaptive filter selection in highly correlated sensing architectures. Examples of subpar reconstructions when using all 25 filters can be viewed in Figure S3. We stress that, as it is currently, the filter selection algorithm could not be used in real-time to determine an appropriate subset per analyzed spectrum, unless the RMSE (Root Mean Square Error) were to be switched with another value, such as the residuals of the convex optimization operation or another figure of merit. However, it could still be possible to use this peculiarity of the system to individuate optimal subset per spectral type (differing in bandwidth, peak position, etc.) by training on known groups of representative spectra. Across a diverse set of experimental spectra—including broad and narrowband signals—we obtain relative reconstruction errors as low as a few percent, demonstrating accurate recovery of spectral shape, bandwidth, and peak position over a 400 nm-wide visible range. The reconstructed spectra in Figure 6 demonstrate that the DCT-based regularization reliably recovers the global spectral features—including peak wavelength and bandwidth—

21951071, 0, Downloaded from https://advanced.onlinelibrary.wiley.com/doi/10.1002/adom.71918 by CochraneItalia, Wiley Online Library on [23/10/2026]. See the Terms and Conditions (https://onlinelibrary.wiley.com/terms-and-conditions) on Wiley Online Library for rules of use; OA articles are governed by the applicable Creative Commons License

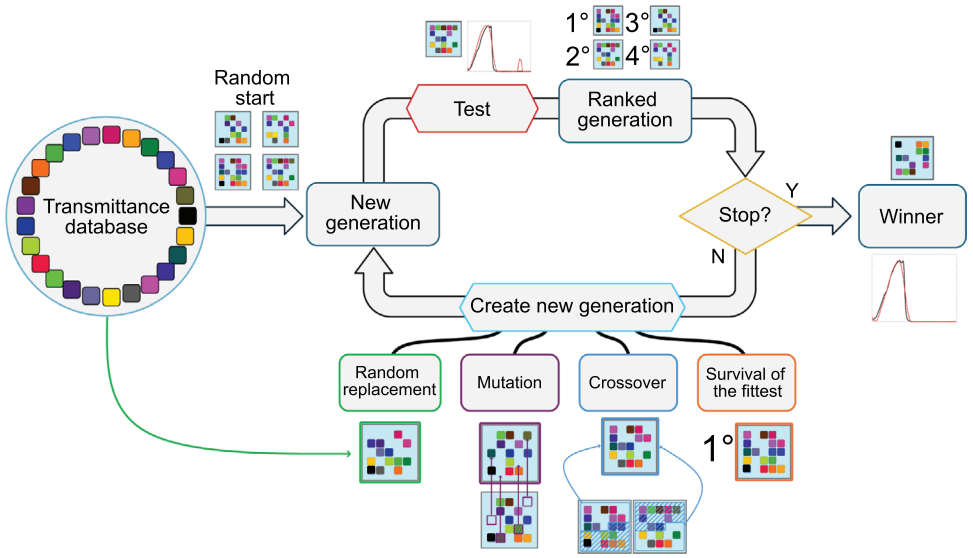

FIGURE 5 | The basis of a genetic algorithm is the generation loop, which scores the elements of each generation and uses the better ones to create the next generation. This loop is initialized by creating the first generation at random. In our case, the population of elements is composed of the possible combinations of filters, or "sets". Each set is scored depending on how well it reconstructs the target spectra, which is quantified by the Root Mean Square Error (RMSE) between the reconstruction and the ground truth. Once scored, the next generation is created by 1) keeping the best-scoring element (survival of the fittest), 2) combining two sets by taking half the filters from one, half from the other (crossover), 3) modifying some filters of a set (mutation), and 4) filling all remaining spots of the generation with new, randomly constructed filter sets. Once the stop criterion has been met, by reaching either a target RMSE or the iteration limit, the best-scoring set is utilized for the final reconstruction.

even when fine spectral details are partially smoothed. This behavior highlights the intrinsic trade-off of the chosen basis: while it limits the reconstruction of sharp spectral edges, it enables robust recovery using a remarkably small number of filters over a broad spectral range. We have estimated the spectral resolution of our system to be 5 nm under noiseless conditions, and 10 nm for noisy conditions, by simulating the reconstruction of two close, narrow Gaussian peaks (Figure S4). However, we question whether this use of Rayleigh's criterion is applicable to reconstructive spectroscopy, as it was formulated around the effects of diffraction and the locality of the resulting signal, neither of which are present in our system. Therefore, we have devised a second method: we estimate the experimental resolving power of our spectrometer by considering the FWHM of the narrowest reconstructed peaks as well as the average size of missed features in broadband signals (i.e., the second peak in Figure 6c). This results in a wavelength-dependent value of, on average, 10 nm; further explanation of this method and our choice of it over Rayleigh's criterion can be found in Section S5. Overall, the combination of smooth interferometric filters, adaptive subset selection, and a-priori calibration enables high-fidelity spectral reconstruction despite strong correlation among encoding elements, contrary to the prevailing assumption that low correlation is a prerequisite for reconstructive spectroscopy.

An important challenge in reconstructive spectroscopy is the ability to reconstruct spectra that encode similar distributions of intensities, as this could lead to solutions closer to each other compared to the relative ground truths. To test the ability of our system in this regard, we have reconstructed the fluorescence of two phosphorescence signals with high overlap in signal over the 500 to 650 nanometer range (Figure 7). Their measured intensity values, normalized by the unfiltered intensity, are, on average, within a three percent difference of each other, thus showing high overlap in encoded data.

We achieved this result by following the procedure illustrated beforehand, except for the convex optimization problem, which was modified to minimize the solution's L2 norm on its first and second derivatives instead of its sparsity in the DCT basis. This result demonstrates that our system can differentiate between highly similar broadband signals and represents a successful stress test of broadband discrimination often lacking in current reconstructive spectroscopy literature. A further practical example is provided in Figure S10, where we report the reconstruction of reflectance spectra measured from colored paper samples.

3 | Conclusion

In this work, we have demonstrated that high-fidelity spectral reconstruction can be achieved using arrays of inkjet-printed interferometric filters that are far simpler, cheaper, and more scalable than the optical encoders commonly reported in the literature (see Table S1). The minimalistic tri-layer architecture makes them easier to customize for specific applications or spectral ranges, and the inkjet manufacturing method has great potential for compact and deployable spectroscopic systems as it enables inexpensive, large-scale, micrometer-precise production.

Beyond the specific device implementation, our results deviate from a widely held assumption in reconstructive spectroscopy: that accurate reconstruction requires encoding elements with low mutual correlation. Instead, we find that smooth, highly correlated filter responses, when combined with adaptive subset selection and data-efficient reconstruction, can potentially

21951071, 0, Downloaded from https://advanced.onlinelibrary.wiley.com/doi/10.1002/adom.71918 by CochraneItalia, Wiley Online Library on [23/10/2026]. See the Terms and Conditions (https://onlinelibrary.wiley.com/terms-and-conditions) on Wiley Online Library for rules of use; OA articles are governed by the applicable Creative Commons License

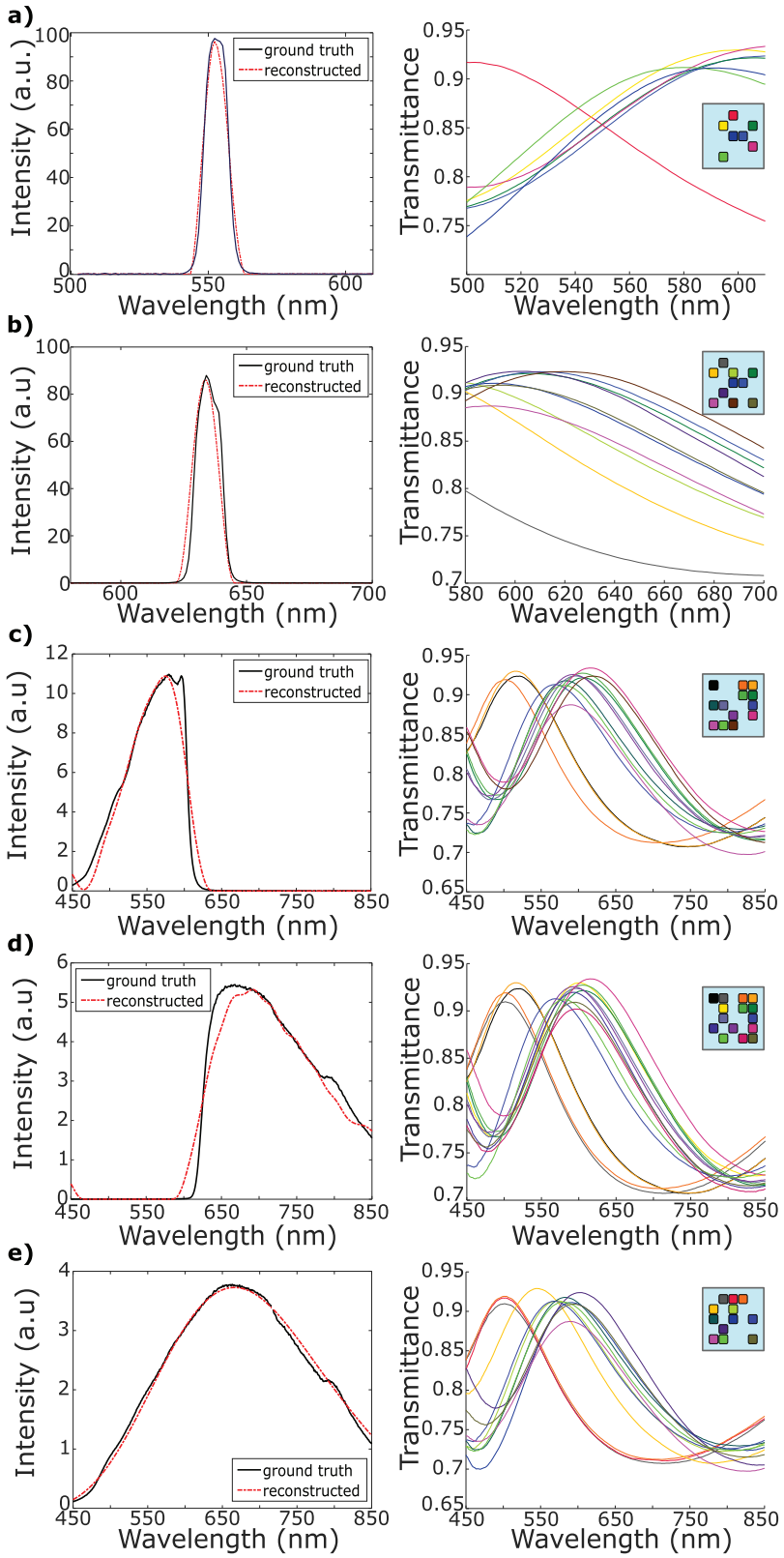

FIGURE 6 | The reconstruction of the transmission spectra of a narrowband signal in the green spectral region (a), a narrowband signal in the red spectral region (b), two broadband signals peaked in the same spectral regions (c, d), and a white broadband signal (e) are shown together with the corresponding filter transmittances selected by the genetic algorithm. Improved reconstruction performance is observed in the green spectral region, which is attributed to the greater diversity of filter transmittance shapes in this wavelength range. The RRMSE for the respective reconstructions are: (a) 4.9% (b) 5.4% (c) 2.4% (d) 4.5% (e) 0.17%.

21951071, 0, Downloaded from https://advanced.onlinelibrary.wiley.com/doi/10.1002/adom.71918 by CochraneItalia, Wiley Online Library on [23/10/2026]. See the Terms and Conditions (https://onlinelibrary.wiley.com/terms-and-conditions) on Wiley Online Library for rules of use; OA articles are governed by the applicable Creative Commons License

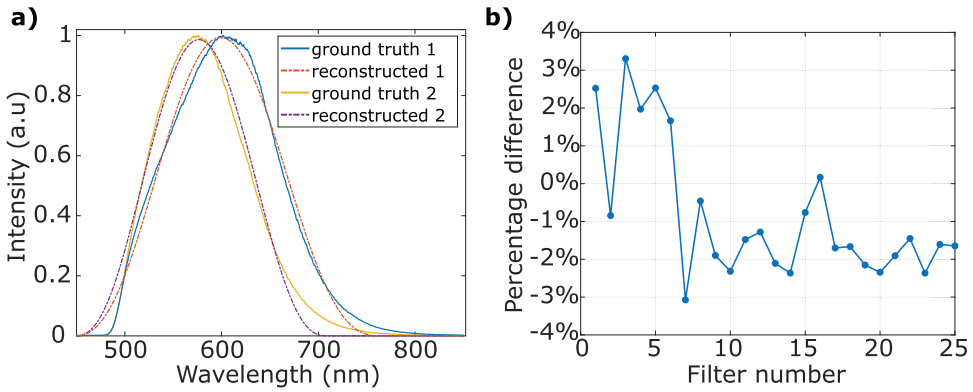

FIGURE 7 | (a) The peak wavelength of the two target spectra differs only by 25 nanometers, the first being 575 nm and the second being 600 nm, while their full widths at half maximum are 115 and 140 nm. (b) The percentage difference between intensity values for each filter. For the first ground truth, a subset of thirteen filters was chosen for reconstruction, for the second ground truth, a subset of seventeen. The relative transmittance functions can be viewed in Figure S9.

outperform larger, generalist filter sets, with different spectra best reconstructed using different numbers and combinations of filters. This observation suggests an alternative design for reconstructive spectrometers, in which a large library of simple, application-tailored encoding elements is combined with adaptive computational selection, either guided by a previous calibration or carried out in real time. The numerical calibration of the regularization parameter would add to this design, allowing the selection of its value with minimal a priori information, easing the practical deployment of the system. Together, these results outline new avenues for scalable, adaptive, and cost-effective spectral sensing across a wide range of scientific and technological applications.

Looking even further into the future, the proposed techniques can be scaled up to a reconstructive hyperspectral camera by miniaturizing the encoder matrix. Here, the filter pattern would be repeated periodically to cover the sensor of a commercial camera, modulating the incident light. Consequently, each unitary filter matrix would encode information onto the group of pixels behind it. By postprocessing the intensities from each group, a hyperspectral image of the framed object could be reconstructed. Taking inspiration from the improvement observed from filter subset selection, an additional layer could be added to the system to block light from channels that have been excluded. This control layer could, as an example, be constructed of nematic liquid crystals, functioning akin to a Liquid Crystal Display.

4 | Experimental Methods

4.1 | Filter Design and Fabrication

The tri-layer designs were planned using the *tmmnlay* [36] library for Python, which allows for the simulation of the optical properties of multi-layer materials. The numerical transmittances obtained were tested on publicly available spectra databases to ascertain their reconstruction capabilities before printing. The optical filters were then fabricated using an inkjet printer (PixDro LP50) equipped with 10 pL cartridges (Fujifilm Dimatix), following the method described by Jin et al. [37], and summarized in Figure S11. To print each layer, customized printing waveforms were applied at jetting frequencies ranging from 1 to 3 kHz. Ink droplets were deposited onto glass substrates at varying printing resolutions under ambient conditions (21°C–22°C, 40%–50% humidity). Layers with high and low refractive indices are printed alternately, each layer being between 50 nm and 150 nm thick, for a total of three layers per filter. The high- and low-refractive index inks were prepared using titania and silica nanoparticles, respectively, dispersed in 2-propoxyethanol and 1,3-dimethoxybenzene (both from Sigma–Aldrich). Ink concentrations were 1.8 wt.% for the high-index and 3 wt.% for the low-index formulation. Prior to use, both inks were filtered through 0.2 µm PTFE (polytetrafluoroethylene) membranes. The printing results in thin, multi-layered filters of alternating materials, which, depending on the thickness of each layer, modulate the light through interferometric effects. The high average transmittance allowed by interferential filters enables high SNRs, and their shape can be tuned by changing only a few parameters (material and thickness of each layer), making the system simple to interface with and tailorable to specific use cases.

4.2 | Numerical Calibration of Regularization Coefficient

To predict the optimal γ values for different types of spectra, we created a database of simulated Gaussian spectra of different bandwidths and peak wavelengths. For each combination of these two parameters, we calculated the vector of transmitted intensities by the filter matrix, then adding a noise level of 35 dB SNR, mimicking our experimental setup. We ran the *dlib* global optimizer over the reconstruction algorithm to find the optimal γ values for multiple noise realizations, finding the averaged values shown in Figures 3 and 4. The *dlib* global optimizer was selected as it requires no choice of initial guess, making the optimization process as unbiased as possible.

4.3 | Experimental Measurement

The optical filters were mounted on an automated x-y translation stage to minimize repositioning errors during the several measurement cycles. The fiber emission of the white light

21951071, 0, Downloaded from https://advanced.onlinelibrary.wiley.com/doi/10.1002/adom.71918 by Cochraneltalia, Wiley Online Library on [23/10/2026]. See the Terms and Conditions (https://onlinelibrary.wiley.com/terms-and-conditions) on Wiley Online Library for rules of use; OA articles are governed by the applicable Creative Commons License

source (OceanOptics LS-1) was collected and collimated by a 10x microscope objective. The beam had a spot size of ∼1 mm in diameter. The spectral transmittances of the filters at normal incidence were measured with a commercial spectrometer (Ocean Optics Red Tide USB650). The spectral signals were obtained by filtering the white lamp with different commercial filters, narrow bandpass filters for the narrow signals and either longpass or shortpass filters for the broader signals. The transmitted intensities were measured using a grayscale camera (an IDS UI-3060CP-M-GL). The spectra of the ground truths have also been characterized with the in-fiber spectrometer for comparison with their reconstructions.

4.4 | Filter Selection via a Genetic Algorithm

The evaluation was carried out on groups of elements, called generations, each containing ten filter sets. The first generation contained one set containing all twenty-five unique filters and nine randomly created sets. In every step of the algorithm, each set of the current generation was evaluated and scored on its reconstruction performance. The next generation was then created from the current, ranked generation by a series of operations: (i) The top scorer was kept for the next generation (survival of the fittest); (ii) Four sets were created by combining the elements of sets of the previous generation (crossover); (iii) One set was created by randomly changing some filters of a previous set (mutation); (iv) The remaining four sets were created by randomly choosing filters from the database (random replacement). The higher the score of a set within a generation, the more likely it is to be chosen for the crossover and mutation operations to improve promising sets further. Conversely, sets created by random replacement were used to probe the combination space as widely as possible. To optimize both the reconstruction quality as well as the optimal number of filters, our genetic functions operated in a non-intuitive manner: crossover, mutation, and random replacement were able to generate filter sets that contained the same filter multiple times, however, when reconstructing a spectrum, each filter in the set was considered only once. Since duplicates were not considered in the reconstruction, a set with more duplicates had operationally a lower number of filters than a set with less duplicates. Thus, the algorithm would reduce the number of effective filters if this improved the reconstruction quality.

Author Contributions

Leonardo Baini: Writing – original draft, investigation, methodology, software, visualization, formal analysis, Writing – review and editing. **Qihao Jin**: resources, validation, investigation, writing – review and editing. **Qiaoshuang Zhang**: resources, validation, investigation, writing – review and editing. **Guillaume Gomard**: supervision, validation, writing – review and editing, project administration. **Ulrich Lemmer**: supervision, funding acquisition, project administration, writing – review and editing. **Paolo Bartolini**: investigation, writing – review and editing. **Andrea Taschin**: investigation, writing – review and editing. **Diederik S. Wiersma**: writing – review and editing, project administration, supervision, funding acquisition. **Renato Torre**: writing – review and editing, supervision, funding acquisition. **Alice Boschetti**: writing – review and editing, conceptualization, supervision, methodology, writing – original draft, investigation, funding acquisition, formal analysis, software, project administration.

Acknowledgements

The work has been financially supported by the project CNR-FOE-LENS, by the European Union's NextGeneration EU Programme with the I-PHOQS Infrastructure [IR0000016, ID D2B8D520, CUP B53C22001750006]. L.B. gratefully acknowledges the financial support of the Italian Ministry of University and Research for the PhD program DM 630/2024, co-funded under the PNRR.

Open access publishing facilitated by Universita degli Studi di Firenze, as part of the Wiley - CRUI-CARE agreement.

Conflicts of Interest

The authors declare no conflicts of interest.

Code Availability

The custom codes that support the current study are available from the corresponding authors on request.

Data Availability Statement

The data that support the findings of this study are available from the corresponding author upon reasonable request.

References

1. Q. Xue, Y. Yang, W. Ma, et al., "Advances in Miniaturized Computational Spectrometers," *Advanced Science* 11, no. 47 (2024): 2404448, https://doi.org/10.1002/advs.202404448.

2. E. Huang, Q. Ma, and Z. Liu, "Etalon Array Reconstructive Spectrometry," *Scientific Reports* 7, no. 1 (2017): 40693, https://doi.org/10.1038/srep40693.

3. M. Yako, Y. Yamaoka, T. Kiyohara, et al., "Video-Rate Hyperspectral Camera Based on a CMOS-Compatible Random Array of Fabry–Pérot Filters," *Nature Photonics* 17, no. 3 (2023): 218–223, https://doi.org/10.1038/s41566-022-01141-5.

4. J. Bao and M. Bawendi, "A Colloidal Quantum Dot Spectrometer," *Nature* 523, no. 7558 (2015): 67–70, https://doi.org/10.1038/nature14576.

5. G. Mu, C. Bi, J. Zou, Y. Liu, Q. Hao, and X. Tang, "Hyperspectral Quantum-Dot Image Sensors via In-Pixel Reconfigurable Band-Alignment," *Nature Photonics* 20, no. 5 (2026): 523–531, https://doi.org/10.1038/s41566-026-01860-z.

6. C. Kim, W. B. Lee, S. K. Lee, Y. T. Lee, and H. N. Lee, "Fabrication of 2D Thin-Film Filter-Array for Compressive Sensing Spectroscopy," *Optics and Lasers in Engineering* 115 (2019): 53–58, https://doi.org/10.1016/j.optlaseng.2018.10.018.

7. J. Yang, K. Cui, X. Cai, et al., "Ultraspectral Imaging Based on Metasurfaces With Freeform Shaped Meta-Atoms," *Laser & Photonics Reviews* 16, no. 7 (2022): 2100663, https://doi.org/10.1002/lpor.202100663.

8. J. Xiong, X. Cai, K. Cui, et al., "Dynamic Brain Spectrum Acquired by a Real-Time Ultraspectral Imaging Chip With Reconfigurable Metasurfaces," *Optica* 9, no. 5 (2022): 461–468, https://doi.org/10.1364/OPTICA.440013.

9. Q. Zhang, P. Lin, C. Wang, et al., "Neural-Optic Co-Designed Polarization-Multiplexed Metalens for Compact Computational Spectral Imaging," *Laser & Photonics Reviews* 18, no. 8 (2024): 2400187, https://doi.org/10.1002/lpor.202400187.

10. Z. Yang, T. Albrow-Owen, H. Cui, et al., "Single-Nanowire Spectrometers," *Science* 365, no. 6457 (2019): 1017–1020, https://doi.org/10.1126/science.aax8814.

11. Z. Zhou, Y. Zhang, Y. Xie, et al., "Electrically Tunable Planar Liquid-Crystal Singlets for Simultaneous Spectrometry and Imaging," *Light:*

21951071, 0, Downloaded from https://advanced.onlinelibrary.wiley.com/doi/10.1002/adom.71918 by Cochraneltalia, Wiley Online Library on [23/10/2026]. See the Terms and Conditions (https://onlinelibrary.wiley.com/terms-and-conditions) on Wiley Online Library for rules of use; OA articles are governed by the applicable Creative Commons License

Science & Applications 13, no. 1 (2024): 242, https://doi.org/10.1038/s41377-024-01608-w.

12. X. Wang, Z. Ruan, F. Huang, et al., "Low-Power and Fast-Scan Reconstructive Spectrometer Chip With pm Resolution on Thin-Film Lithium Niobate," *Laser & Photonics Reviews* 19, no. 15 (2025): 2500163, https://doi.org/10.1002/lpor.202500163.

13. B. Redding, S. F. Liew, R. Sarma, and H. Cao, "Compact Spectrometer Based on a Disordered Photonic Chip," *Nature Photonics* 7, no. 9 (2013): 746–751, https://doi.org/10.1038/nphoton.2013.190.

14. C. Yao, K. Xu, T. Lin, et al., "Benchmarking Reconstructive Spectrometer With Multiresonant Cavities," *ACS Photonics* 11, no. 9 (2024): 3730–3740, https://doi.org/10.1021/acsphotonics.4c00915.

15. G. Cai, Y. Li, Y. Zhang, et al., "Compact Angle-Resolved Metasurface Spectrometer," *Nature Materials* 23, no. 1 (2024): 71–78, https://doi.org/10.1038/s41563-023-01710-1.

16. D. S. Bhatti, J. Lee, C. Kim, D. Park, J. Lee, and H. N. Lee, "Deep Learning-Based Single-Shot Computational Spectrometer Using Multilayer Thin Films," *Scientific Reports* 15, no. 1 (2025): 21232, https://doi.org/10.1038/s41598-025-06691-6.

17. J. Oliver, W. B. Lee, and H. N. Lee, "Filters With Random Transmittance for Improving Resolution in Filter-Array-Based Spectrometers," *Optics Express* 21, no. 4 (2013): 3969–3989, https://doi.org/10.1364/OE.21.003969.

18. N. Sharma, G. Kumar, V. Garg, G. Mote, and S. Gupta, "Reconstructive Spectrometer Using a Photonic Crystal Cavity," *Optics Express* 29, no. 17 (2021): 26645–26657, https://doi.org/10.1364/OE.432831.

19. Z. Cheng, Y. Zhao, J. Zhang, et al., "Generalized Modular Spectrometers Combining a Compact Nanobeam Microcavity and Computational Reconstruction," *ACS Photonics* 9, no. 1 (2021): 74–81, https://doi.org/10.1021/acsphotonics.1c00719.

20. V. Wang, S. Z. Uddin, J. Park, and A. Javey, "Highly Multicolored Light-Emitting Arrays for Compressive Spectroscopy," *Science Advances* 9, no. 16 (2023): adg1607, https://doi.org/10.1126/sciadv.adg1607.

21. M. Rani, S. B. Dhok, and R. B. Deshmukh, "A Systematic Review of Compressive Sensing: Concepts, Implementations and Applications," *IEEE Access* 6 (2018): 4875–4894, https://doi.org/10.1109/ACCESS.2018.2793851.

22. J. Oliver, W. Lee, S. Park, and H. N. Lee, "Improving Resolution of Miniature Spectrometers by Exploiting Sparse Nature of Signals," *Optics Express* 20, no. 3 (2012): 2613–2625, https://doi.org/10.1364/OE.20.002613.

23. D. Liu and Z. Li, "New Nano-Structure Spectrometer by Introducing Gold Nano-Pillars for Spectral Reconstruction Ability Improvement," *Optics Communications* 502 (2022): 127419, https://doi.org/10.1016/j.optcom.2021.127419.

24. Z. Guo, L. Zhang, and D. Dai, "Ultracompact Spatial Speckle Reconstructive Spectrometer Based on a Waveguide Corner With Chaotic Reflection," *ACS Photonics* 12, no. 4 (2025): 1981–1988, https://doi.org/10.1021/acsphotonics.4c02401.

25. H. Li, L. Bian, K. Gu, et al., "A Near-Infrared Miniature Quantum Dot Spectrometer," *Advanced Optical Materials* 9, no. 15 (2021): 2100376, https://doi.org/10.1002/adom.202100376.

26. C. Kim, P. Ni, K. R. Lee, and H. N. Lee, "Mass Production-Enabled Computational Spectrometers Based on Multilayer Thin Films," *Scientific Reports* 12, no. 1 (2022): 4053, https://doi.org/10.1038/s41598-022-08037-y.

27. T. L. Vasconcelos, S. N. Vladimirov, T. Pucher, et al., "Strain-Engineered Adaptive 2D Photodetectors: A New Approach to Miniaturized Reconstructive Spectrometry," *Nano Letters* 25, no. 29 (2025): 11333–11339, https://doi.org/10.1021/acs.nanolett.5c02470.

28. D. L. Donoho, "For Most Large Underdetermined Systems of Linear Equations the Minimal ℓ1 -Norm Solution Is Also the Sparsest Solution," *Communications on Pure and Applied Mathematics* 59, no. 6 (2006): 797–829, https://doi.org/10.1002/cpa.20132.

29. E. Candes and J. Romberg, "Sparsity and Incoherence in Compressive Sampling," *Inverse Problems* 23, no. 3 (2007): 969–985, https://doi.org/10.1088/0266-5611/23/3/008.

30. E. Andries and S. Martin, "Sparse Methods in Spectroscopy: An Introduction, Overview, and Perspective," *Applied Spectroscopy* 67, no. 6 (2013): 579–593, https://doi.org/10.1366/13-07021.

31. S. Bourguignon, D. Mary, and É. Slezak, "Restoration of Astrophysical Spectra With Sparsity Constraints: Models and Algorithms," *IEEE Journal of Selected Topics in Signal Processing* 5, no. 5 (2011): 1002–1013, https://doi.org/10.1109/JSTSP.2011.2147278.

32. C. Yao, K. Xu, W. Zhang, M. Chen, Q. Cheng, and R. Penty, "Integrated Reconstructive Spectrometer With Programmable Photonic Circuits," *Nature Communications* 14, no. 1 (2023): 6376, https://doi.org/10.1038/s41467-023-42197-3.

33. K. Okamoto and B. Q. Li, "Optimal Numerical Methods for Choosing an Optimal Regularization Parameter," *Numerical Heat Transfer, Part B: Fundamentals* 51, no. 6 (2007): 515–533, https://doi.org/10.1080/10407790601128592.

34. D. E. King, "Dlib-ml: A Machine Learning Toolkit," *The Journal of Machine Learning Research* 10 (2009): 1755–1758, https://dl.acm.org/doi/abs/10.5555/1577069.1755843.

35. B. Arad and O. Ben-Shahar, "Filter Selection for Hyperspectral Estimation," in *Proc. of the IEEE International Conference on Computer Vision (ICCV)*, Venice, Italy (2017), 3153–3161, https://doi.org/10.1109/ICCV.2017.342.

36. O. P. Rodríguez, "tmmnlay", GitHub repository, (2020) https://github.com/ovidiopr/tmmnlay (accessed November 2024).

37. Q. Jin, Q. Zhang, C. Rainer, et al., "Inkjet-Printed Optical Interference Filters," *Nature Communications* 15, no. 1 (2024): 3372, https://doi.org/10.1038/s41467-024-47086-x.

Supporting Information

Additional supporting information can be found online in the Supporting Information section.

Supporting File 1: adom71918-sup-0001-SuppMat.docx

21951071, 0, Downloaded from https://advanced.onlinelibrary.wiley.com/doi/10.1002/adom.71918 by CochraneItalia, Wiley Online Library on [23/10/2026]. See the Terms and Conditions (https://onlinelibrary.wiley.com/terms-and-conditions) on Wiley Online Library for rules of use; OA articles are governed by the applicable Creative Commons License